Excitation spectroscopy in multispectral optical fluorescence tomography: methodology, feasibility, and computer simulation studies

Abhijit J Chaudhari[1,4], **Sangtae Ahn**[2], **Richard Levenson**[3], **Ramsey D Badawi**[4], **Simon R Cherry**[1], and **Richard M Leahy**[2]

Abhijit J Chaudhari: ajchaudhari@ucdavis.edu; Sangtae Ahn: ; Richard Levenson: ; Ramsey D Badawi: ; Simon R Cherry: ; Richard M Leahy: leahy@sipi.usc.edu

[1]Department of Biomedical Engineering, University of California-Davis, Davis, CA 95616, USA

[2]Signal and Image Processing Institute, University of Southern California, Los Angeles, CA 90089, USA

[3]Cambridge Research Instruments, Inc., Woburn, MA 01801, USA

[4]Department of Radiology, UC Davis Medical Center, Sacramento, CA 95817, USA

Abstract

Molecular probes used for *in vivo* Optical Fluorescence Tomography (OFT) studies in small animals are typically chosen such that their emission spectra lie in the 680–850 nm wavelength range. This is because tissue attenuation in this spectral band is relatively low, allowing optical photons even from deep sites in tissue to reach the animal surface, and consequently be detected by a CCD camera. The wavelength dependence of tissue optical properties within the 680–850 nm band can be exploited for emitted light by measuring fluorescent data via multispectral approaches and incorporating the spectral dependence of these optical properties into the OFT inverse problem - that of reconstructing underlying 3D fluorescent probe distributions from optical data collected on the animal surface. However, in the aforementioned spectral band, due to only small variations in the tissue optical properties, multispectral emission data, though superior for image reconstruction compared to achromatic data, tend to be somewhat redundant. A different spectral approach for OFT is to capitalize on the larger variations in the optical properties of tissue for excitation photons than for the emission photons by using excitation at multiple wavelengths as a means of decoding source depth in tissue. The full potential of spectral approaches in OFT can be realized by a synergistic combination of these two approaches, that is, exciting the underlying fluorescent probe at multiple wavelengths and measuring emission data multispectrally. In this paper, we describe a method that incorporates both excitation as well as emission spectral information into the OFT inverse problem. We describe a linear algebraic formulation of the multiple wavelength illumination - multispectral detection (MWI-MD) forward model for OFT and compare it to models that use only excitation at multiple wavelengths or those that use only multispectral detection techniques. This study is carried out in a realistic inhomogeneous mouse atlas using singular value decomposition and analysis of reconstructed spatial resolution versus noise. For simplicity, quantitative results have been shown for one representative fluorescent probe (Alexa 700®) and effects due to tissue autofluorescence have not been taken into account. We also demonstrate the performance of our method for 3D reconstruction of tumors in a simulated mouse model of metastatic human hepatocellular carcinoma.

1. Introduction

For Optical Fluorescence Tomography (OFT) in small animals, a large number of near-infrared (NIR) photons emitted by fluorescent sources even at deep sites in tissue reach the animal

surface due to short optical path-lengths and low tissue attenuation (Chance 1991, Weissleder et al. 1999, Ntziachristos and Weissleder 2001). Consequently, 3D tomographic reconstruction of fluorescent source distribution using non-ionizing NIR radiation becomes possible (Weissleder and Ntziachristos 2003, Cherry 2004, Ntziachristos et al. 2005). A large number of novel fluorescent dyes and proteins probing cellular and sub-cellular processes have become available (Neefjes and Dantuma 2004, Giepmans et al. 2006, Adams et al. 2007). These advancements coupled with the development of 3D tomographic small animal imaging systems by academicians (Ntziachristos and Weissleder 2002, Patwardhan et al. 2005, Joshi et al. 2006a, Hassan et al. 2007, Kumar et al. 2008) and by industries, e.g. IVIS 3D® (Caliper Life Sciences, Hopkinton, MA, USA), eXplore Optix MX (Advanced Research Technologies-GE Healthcare), FMT™ 2500 (VisEn Medical, Inc., Bedford, MA, USA) etc., have facilitated both applications of OFT for early detection and rapid screening in mouse models of disease, as well as for detailed investigation of molecular function (Massoud and Gambhir 2003, Ntziachristos 2006, Weber et al. 2008, Luker and Luker 2008).

In this paper, we focus on continuous-wave (CW) domain illumination and detection techniques for OFT (Ntziachristos et al. 2005) with non-contact tomographic measurements (Schulz et al. 2004, Joshi et al. 2006b). Light propagation for OFT in CW-domain can be modeled by three steps:

A. excitation photon transport from the external illumination source to the animal surface and then to the site of the underlying fluorescent probe,

B. propagation of emitted photons from the fluorescent source to the animal surface, and

C. mapping of the photon fluence from the animal surface to the CCD camera.

The coupled radiative mapping in steps (A) and (B), whose mathematical description in biological tissue can be given by the radiative transport equation (RTE), constitutes the OFT 'forward' model (Arridge et al. 1993, Klose and Hielscher 2003). OFT studies based on the solution of the RTE have been carried out (Klose et al. 2005, Joshi et al. 2008). For practical biomedical imaging applications, however, the RTE-based solution is computationally expensive (Ntziachristos 2006). The steady-state diffusion equation (DE) with appropriate boundary conditions may be used as a practical approximation to the RTE (Patterson et al. 1992, Arridge and Hebden 1997, Paithankar et al. 1997). However, concerns regarding the applicability of this approximation to small animal volumes where source-detector separation distances are small and void, non-diffusive regions are present exist (Hielscher 2005). Ren et al. (2007) compared RTE-based and diffusion approximation-based optical tomographic reconstructions in small domains. They found that RTE-based solutions were more quantitatively accurate, while the diffusion approximation-based solutions were more practical computationally. Combined radiosity-diffusion models have also been proposed in the literature (Dehghani et al. 2000). The issue of how well the DE approximates the RTE is not considered in our paper. Owing to the large number of image reconstructions carried out in our paper, we have used the diffusion approximation for generating the forward models, and thus, our results are relevant when this approximation is sufficiently accurate.

The surface geometry and internal anatomy of the animal needs to be estimated before the OFT forward model can be accurately solved. Direct methods for this estimation involve scanning the animal using an anatomical imaging modality, e.g. computed tomography (CT) or magnetic resonance imaging (MRI), before or after the optical scan without moving the animal (Ntziachristos et al. 2002, Chaudhari et al. 2005, Lv et al. 2006, Guven et al. 2007). Alternatively, the animal's surface topography can be estimated by all-optical methods, for example, by using photogrammetry systems (Ripoll et al. 2003), by utilizing systems that project structured light on the animal surface (Rice et al. 2006), by shadowgrammetric techniques (Meyer et al. 2007) or via 3D volume carving (Lasser et al. 2008). Once the surface

topography is known, the internal organ boundaries may be estimated using a deformable mouse atlas (Wang et al. 2006, Chaudhari et al. 2007). Alternatively, data normalization techniques may be used to reduce the impact of tissue heterogeneity (Soubret et al. 2005, Axelsson et al. 2007). Step (C) is typically modeled using the estimated surface geometry with free-space optics formulae and assuming that the mouse surface is lambertian (Ripoll and Ntziachristos 2004).

In the NIR region, low attenuation of emitted photons is a consequence of a low optical absorption coefficient μ_a. The reduced scattering coefficient μ'_s is high compared to μ_a in this region, but is lower than its own value for blue light. Since both μ_a and μ'_s are functions of wavelength λ (Cheong et al. 1990), for step (B), tissue acts like a spectral filter for emitted photons causing the wavelength spectra measured at the tissue surface for a given optical source to vary depending on its depth in tissue (Swartling et al. 2005, Zacharakis et al. 2005, Zavattini et al. 2006). This property has been exploited in Bioluminescence Tomography (BLT) by the use of multispectral or hyperspectral data measurement techniques that lead to better conditioning of the forward models and yield reasonably accurate 3D source reconstruction results for *in vivo* studies compared to those generated using achromatic or monochromatic data sets (Chaudhari et al. 2005, Cong and Wang 2006, Dehghani et al. 2006, Kuo et al. 2007). The imaging window used in these BLT studies was restricted to 550–660 nm corresponding to the emission band for Firefly Luciferase (FFL). These studies concluded that variations in tissue μ_a and μ'_s for individual wavelength bins within the emission band of interest provided a fair amount of independent information that helped in reducing the ill-posedness of the inverse problem. For OFT, fluorescent probes are chosen to have their emission spectrum in the 680–850 nm band where the tissue attenuation is a lot lower than in the 550–660 nm range (Pinaud et al. 2006). Thus, more fluorescent light photons will reach the CCD camera compared to BLT for sources with equivalent strengths (Ntziachristos et al. 2005). While multispectral fluorescent emission data were also found to be helpful in reducing the illconditioning of the OFT inverse problem (Zacharakis et al. 2005, Swartling et al. 2005, Zavattini et al. 2006, Chaudhari 2006), the full potential of spectral approaches has not yet been realized. This is because in the 680–850 nm wavelength band, the variation in μ_a and μ'_s with wavelength is small (Weissleder and Ntziachristos 2003, Bargo et al. 2005). As a consequence, spectral emission data acquired in this band tend to be somewhat redundant.

Step (A) for OFT offers a unique degree-of-freedom unavailable in BLT. The external illumination source may be used to elicit different mappings from the fluorescent source to the animal surface and can provide a way of reducing the ill-posedness of the OFT inverse problem compared to that for BLT (Chang et al. 1997, Ntziachristos et al. 2005). Proposed approaches have investigated parameters based on the nature of the illumination source (e.g. point-like or distributed) and the spatial distribution of the incident illumination light in the imaging field of view for improving the conditioning of the OFT forward problem (Ntziachristos et al. 2004, Godavarty et al. 2004, Pogue et al. 2004, Roy et al. 2006, Joshi et al. 2006b).

Step (A) is also a function of wavelength. Optical property variability for tissue is higher for excitation light compared to emission light (Cheong et al. 1990). This is because the excitation spectrum is blue-shifted compared to the emission spectrum. Thus, illumination at different wavelengths within the excitation band of a fluorophore should correspond to different light propagation functions in tissue at those wavelengths. This multiple wavelength approach for illumination is complementary to multispectral detection. Therefore, the ill-posedness of the OFT inverse problem may potentially be reduced if spectral information from both the excitation and emission domains is combined.

In this paper, we propose a method for OFT that incorporates both excitation and emission spectral information about the underlying fluorescent probe into the tomographic inverse

problem. This paper is organized as follows. We first present a linear algebraic formulation of forward models that allows taking into account excitation at multiple wavelengths and multispectral detection of emission data. Benefits of utilizing both excitation and emission domains for OFT are presented in a singular value decomposition study in the 3D Digimouse atlas (Dogdas et al. 2007), where the conditioning of the forward models listed in table 1 is compared. A regularized pseudo-inverse-based estimator is used for image reconstruction. A comparative study of the resulting spatial resolution and variance for this estimator for the different forward models is also presented. We also show results from a performance evaluation study that demonstrates the application of the proposed method to the reconstruction of primary and secondary tumors in a computer simulated orthotopic mouse model of metastatic human hepatocellular carcinoma (Sun et al. 1996).

2. Methods

2.1. Forward models for OFT

For OFT, the forward problem is to predict the photon fluence measured at the CCD camera plane due to an underlying fluorescent probe distribution inside the 3D animal volume. This model should also account for the excitation of the fluorophore by an external illumination source. Steps (A) and (B) described in section 1 can be modeled using the following coupled equations based on the steady-state DE with a Robin-type boundary condition (Arridge et al. 1993, Patterson and Pogue 1994, Reynolds et al. 1997, Milstein et al. 2003):

$$g(\mathbf{r}, \lambda_i) = D_i \, p(\mathbf{r}, \lambda_i), \tag{1}$$

$$q(\mathbf{r}, \lambda_j) = D_j \, h(\mathbf{r}, \lambda_j), \tag{2}$$

where $D = -\{\nabla \cdot \kappa(\mathbf{r}, \lambda) \nabla - \mu_a(\mathbf{r}, \lambda) c\}$ represents the diffusion operator as a function of wavelength λ and of 3D position $\mathbf{r}$, and D_i and D_j represent the diffusion operators at the excitation wavelength λ_i and emission wavelength λ_j respectively. The term g denotes the photon flux on the animal surface due to the external illumination, p and q denote the incident and emitted flux for a fluorophore in the interior of the animal volume, and h denotes the photon flux inside the volume as well as on the surface. The emitted photon flux $q = \eta p$, where η represents the fluorescence yield. In the equation for D, the diffusion coefficient $\kappa(\mathbf{r})$ is given by the equation

$$\kappa(\mathbf{r}) = \frac{c}{3[\mu_a(\mathbf{r}, \lambda) + \mu'_s(\mathbf{r}, \lambda)]}, \tag{3}$$

where c represents the velocity of light. Numerically, (1) and (2) can either be solved by using a discretized representation of the animal volume and a finite-element based diffusion equation solver (Arridge et al. 1993, Paulsen and Jiang 1995, Joshi et al. 2004, Cong and Wang 2005), or by using analytic approximations of the diffusion equation with appropriate boundary conditions (Haskell et al. 1994, Rice et al. 2001, Soubret et al. 2005, Axelsson et al. 2007). Since the focus of this paper is spectral domain analysis, it is not our goal to evaluate the impact of internal anatomical variability on reconstructed images. Thus, we demonstrate our method using the Digimouse atlas, where internal anatomy is known and optical properties can be assigned to the organs based on published data (Alexandrakis et al. 2005). We solve both (1) and (2) using a tetrahedral representation of the animal volume and the finite element method (FEM) as outlined in Arridge et al. (1999).

Let n represent the total number of possible source locations inside the animal volume and m denote the total number of nodes on the animal surface. Two sets of measurements are carried out. First, a subset of the m surface nodes (w in number) are used for excitation and the other $(m-w)$ nodes are used for detection. Let $\mathbf{A}_1(\lambda_i) \in \mathbb{R}^{n \times w}$ denote the mapping from the w surface nodes to n internal points computed using (1), and $\mathbf{B}_1(\lambda_j) \in \mathbb{R}^{(m-w) \times n}$ denote the mapping from the n internal location to $(m-w)$ surface points computed using (2). The subscripts i and j for λ are used to indicate the excitation and emission wavelengths respectively. If we assume that w nodes are illuminated by an excitation source such that ζ_d, $d = 1, 2, \ldots, w$ denotes the source strength at the w nodes, then the total photon flux at the n internal nodes due to this surface illumination at wavelength λ_i is given by a linear combination of the columns of $\mathbf{A}_1(\lambda_i)$, i.e.

$$\mathbf{a}_1(\lambda_i) = \left(\sum_{d=1}^{w} \zeta_d \mathbf{A}_1^d(\lambda_i) \right),$$

(4)

with $\mathbf{a}_1(\lambda_i) \in \mathbb{R}^n$ and $\mathbf{A}_1^d$ representing the dth column of $\mathbf{A}_1(\lambda_i)$. The combined mapping from the surface excitation to the internal points and then, from the internal points to the surface can be represented as

$$\mathbf{X}_1(\lambda_i, \lambda_j) = \eta \mathbf{B}_1(\lambda_j) \, \mathrm{diag} \, \{\mathbf{a}_1(\lambda_i)\}$$

(5)

with $\mathbf{X}_1(\lambda_i, \lambda_j) \in \mathbb{R}^{(m-w) \times n}$ denoting the mapping with excitation wavelength λ_i and emission wavelength λ_j. The second set of measurements assumes that the remainder $(m-w)$ nodes are used for excitation and w nodes are used as detectors. The corresponding excitation and emission models at λ_i and λ_j are represented by $\mathbf{A}_2(\lambda_i) \in \mathbb{R}^{n \times (m-w)}$ and $\mathbf{B}_2(\lambda_j) \in \mathbb{R}^{w \times n}$ respectively. Let $\mathbf{X}_2(\lambda_i, \lambda_j) \in \mathbb{R}^{w \times n}$ represent the combined mapping analogous to (5) for this second configuration. Thus, the OFT forward model for the complete animal volume for a single illumination wavelength λ_i and a single emission wavelength λ_j can be written as:

$$\mathbf{X}_{ij} = [\mathbf{X}_1^T(\lambda_i, \lambda_j) \, \mathbf{X}_2^T(\lambda_i, \lambda_j)]^T, \ \mathbf{X}_{ij} \in \mathbb{R}^{m \times n}.$$

(6)

The optical setup for the two configurations considered for this paper is shown in figure 1. The mouse surface is assumed to have a total of m surface nodes. One geometrical subset corresponds to uniform illumination (ζ_d = constant for all d) on the top surface at w nodes and detection from the bottom at $(m-w)$ nodes as indicated in figure 1(a), while the second corresponds to uniform illumination on the bottom surface at $(m-w)$ nodes and data acquisition from the top and sides at w nodes. Here, we have considered only two geometrical subsets of the nodes for simplicity. Our mathematical formulation, however, can easily be extended to any number of spatial subsets where (6) would transform to

$$\mathbf{X}_{ij} = \left[\mathbf{X}_1^T(\lambda_i, \lambda_j) \, \mathbf{X}_2^T(\lambda_i, \lambda_j) \cdots \mathbf{X}_f^T(\lambda_i, \lambda_j) \right]^T, \ \mathbf{X}_{ij} \in \mathbb{R}^{m \times n},$$

(7)

where f represents the total number of spatial subsets that span the whole animal surface.

Assume that the fluorophore is excited at y wavelengths over the absorption band and optical data are measured for z spectral bins over the emission wavelength band of interest. Let $\mathbf{s} = [s(\lambda_1) \, s(\lambda_2) \ldots s(\lambda_y)]^T$, $\mathbf{s} \in \mathbb{R}^y$ and $\mathbf{t} = [t(\lambda_1) \, t(\lambda_2) \ldots t(\lambda_z)]^T$, $\mathbf{t} \in \mathbb{R}^z$ represents the absorption and emission spectra respectively of the fluorophore. Then, the four forward models whose

description is given in table 1 are calculated as indicated in . The formulae for the assembly of the SWI-AD and SWI-MD forward models assume that the excitation wavelength is λ_i.

Forward model dimensions are listed in table 2, column 3. The MWI-MD forward model is *y*-times larger than the SWI-MD model and *z*-times larger than the MWI-AD model. In all cases, the data **b** can be represented as a linear transformation on the underlying source distribution **q** (Arridge 1999,Boas et al. 2001,Ntziachristos et al. 2002):

$$\mathbf{b} = X\mathbf{q}, \tag{8}$$

where we have dropped the model descriptor subscript on **X**. The size of **b** for each model will be the row-dimension of that model.

2.2. Inverse methods

The OFT inverse problem is to solve (8) for the unknown source distribution **q** for given data **b**. We focus on least-squares estimation with L^2-norm regularization (Tikhonov and Arsenin 1977):

$$\widehat{\mathbf{q}} = \arg\min_{\mathbf{q}} \Phi(\mathbf{q}), \quad \Phi(\mathbf{q}) = \frac{1}{2}\|\mathbf{b} - X\mathbf{q}\|^2 + \frac{\alpha}{2}\|\mathbf{q}\|^2, \tag{9}$$

where α denotes the regularization parameter that controls the trade-off between spatial resolution and variance. The solution of (9) can be written as (Dahlquist and Bjorck 2008)

$$\widehat{\mathbf{q}} = (\mathbf{X}^{\mathbf{T}}\mathbf{X} + \alpha\mathbf{I})^{-1}\mathbf{X}^{\mathbf{T}}\mathbf{b} = VKV^{\mathbf{T}}\mathbf{X}^{\mathbf{T}}\mathbf{b}, \tag{10}$$

where we have expanded **X** using the SVD as $\mathbf{X} = \mathbf{U}\mathbf{\Sigma}\mathbf{V}^{\mathbf{T}}$, **I** is the identity matrix and

$$\mathbf{K} = \text{diag}\left\{\frac{1}{\sigma_p^2 + \alpha}\right\}, \mathbf{K} \in \mathbb{R}^{n \times n}, p = 1, 2, \ldots, n.$$

Here σ_p^2 denotes the square of the pth singular value. We can interpret $\mathbf{X}^{\mathbf{T}}\mathbf{b}$ as a back-projection of the data into image space, which then is filtered by the $\mathbf{VKV}^{\mathbf{T}}$ operator to give us our estimate **q**^. We have deliberately written (10) in terms of the singular values (σ_p) and the right singular component (**V**) of **X**. This is because the computation of the full **SVD** of **X** is expensive, especially for the MWI-MD model. However, $\mathbf{X}^{\mathbf{T}}\mathbf{X} = \mathbf{V}\mathbf{\Sigma}^2\mathbf{V}^{\mathbf{T}} \in \mathbb{R}^{n \times n}$, where $\mathbf{\Sigma}^2 \in \mathbb{R}^{n \times n}$ is a diagonal matrix containing the squared singular values of **X**. Therefore, the solution in (10) can be found by computing only the right singular vectors of **X**, or equivalently the eigenvectors of $\mathbf{X}^{\mathbf{T}}\mathbf{X}$. Since typically *n* is much smaller than the number of rows in **X**, this is a much less demanding computation than the full SVD of **X**. The major benefit of the regularized pseudo-inverse method for our case, rather than more complex non-linear or constrained estimators, is that it is linear, i.e. the response of the corresponding estimator to arbitrary source distributions can be modeled based on its point spread function alone. Thus, a direct comparison between the forward models becomes relatively straightforward.

2.3. Computation of the forward models

The 3D labeled Digimouse mouse atlas (http://neuroimage.usc.edu/Digimouse.html) was used for all studies. The volumetric tessellation consisted of 306,773 tetrahedral elements connected

at 58,244 nodes. Optical properties as a function of wavelength were assigned to all 17 organs based on published data (Alexandrakis et al. 2005). An example of the organ-wise distribution of optical properties is shown in figure 2(a). The fluorescent probe was assumed to be the Alexa 700® dye whose normalized absorption and emission spectra are shown in figure 2(b). This dye has been used *in vivo* in small animals for imaging metastatic disease (Koenig et al. 2008). The forward models were computed for the optical setup in figure 1. In this setup, the mouse surface was first illuminated uniformly from the top and the photon fluence due to surface illumination was computed at $n = 8903$ internal source nodes (spatial sampling of 1.2 mm) by a fast FEM-based solver (Chaudhari 2006, Ahn et al. 2008a). Then, a mapping from this source grid to $w = 1,455$ nodes on the bottom surface was calculated. This procedure was repeated assuming that the bottom surface of the mouse was illuminated uniformly and that data at $(m - w) = 1,778$ nodes on the top surface were collected. This two-step process was carried out for $y = 6$ illumination wavelength bins (580 nm–680 nm in steps of 20 nm) and for $z = 6$ emission spectral bins (700 nm–800 nm in steps of 20 nm). The SWI-AD and SWI-MD forward models were assembled assuming that the illumination was at $\lambda_i = 680$ nm. The MWI-MD model used data at all six illumination wavelengths and in all six emission bands. While computing the SWI-AD model, we increased the detector spatial sampling by six times so that this model has the same row-dimension as the SWI-MD or the MWI-AD models. All forward models were computed using a custom FEM code written in MATLAB® (The Mathworks, Inc, Natick, MA, USA).

2.4. Singular value decomposition (SVD) study

For each of the forward models, we computed the singular values and the right singular vectors (**V**) of **X**. The singular value spectra were plotted for each model. Comparison of only singular values for OFT may at times be misleading since they only reflect the power along the SVD bases, but do not give any information about the spatial distribution of the corresponding basis vectors (Chaudhari 2006). Therefore, we have also performed a spatial resolution versus variance analysis to further investigate our model comparisons.

2.5. Analysis of reconstructed spatial resolution versus estimator variance

In imaging systems, there inherently exists a trade-off between spatial resolution recovered in the image reconstruction process and the statistical estimator variance, that is, sharpened (higher) spatial resolution comes at the expense of also having higher variance (noise) in the reconstructed image (Alessio and Kinahan 2006). Resolution here is defined as the level of reproduction of spatial detail by the imaging system, while the variance is a measure of how much the estimate varies around its average value. Thus, for a fixed value of variance, an estimator providing the highest spatial resolution is superior. On the other hand, for a fixed value of spatial resolution, the estimator corresponding to the least variance will correspond to a more stable solution. We derive estimators from the computed forward models. Resolution-variance analysis then provides a means for quantitatively comparing these estimators, and in turn, the forward models.

We model the optical data in (8) as

$$\mathbf{b} = Xq + \mathbf{n}, \tag{11}$$

where we assume the noise **n** to be Gaussian and white, such that $\mathbb{E}(\mathbf{n}) = 0$ and cov $(\mathbf{n}) = \mathbb{E}(\mathbf{nn^T}) = \lambda^2 \mathbf{I}$ (Roy et al. 2003). Since $\mathbb{E}(\mathbf{q}\^) = (\mathbf{X^T X} + \alpha \mathbf{I})^{-1} \mathbf{X^T X_q}$, the point spread function at voxel j (PSF$_j$) would be given by

$$\mathrm{PSF}_j = (\mathbf{X^T X} + \alpha \mathbf{I})^{-1} \mathbf{X^T X e}_j = \mathbf{V} \, \mathrm{diag} \left\{ \frac{\sigma_p^2}{\sigma_p^2 + \alpha} \right\} \mathbf{V^T e}_j,$$

(12)

where $\mathbf{e}_j$ is an elementary vector with value 1 at voxel j and $p = 1, 2, \ldots, n$. The spatial resolution for a source at the jth voxel can be defined as the full width at half maximum (FWHM) of the PSF. The total variance, summed over all voxels, is given by:

$$\sum_{p=1}^{n} \mathrm{var}\,(\widehat{q_p}) = \lambda^2 \mathrm{Tr} \left[\mathbf{V} \, \mathrm{diag} \left\{ \frac{\sigma_p^2}{(\sigma_p^2 + \alpha)^2} \right\} \mathbf{V^T} \right].$$

(13)

We chose 100 representative source locations that were at least 3 mm deep in tissue. The source distribution was reconstructed using (10) and the corresponding spatial resolution (averaged over the axial, sagittal and coronal directions) and total variance summed over all voxels were computed. The regularization parameter α was varied from 10^{-6} to 10^{-13} in steps of 10^{-1}. The spatial resolutions computed for all 100 sources for a fixed regularization parameter were averaged. For realistic simulations, we added zero-mean Gaussian noise to the data such that the signal-to-noise ratio (SNR) for MWI-MD was 100 (20 dB). This value was chosen based on the performance of currently available systems (Ntziachristos and Weissleder 2002). For a fair comparison, since it takes six times longer to acquire data for MWI-MD compared to SWI-MD or MWI-AD (assuming the scan times for each spectral bin for excitation and emission are the same), we assume that data for the latter two were measured in a six times longer scan. This assumption then decreased the noise variance λ^2 for the SWI-MD and MWI-AD models by a factor of 6. This same assumption also decreased the noise variance λ^2 by a factor of 36 for the SWI-AD case. With these consideration, the SNRs for the models became 100 or 20 dB (MWI-MD), 600 or 27.8 dB (SWI-MD and MWI-AD), and 3600 or 35.5 dB (SWI-AD). We also assumed that the signal strength remained the same over the duration of the scan.

2.6. Imaging comparisons in realistic mouse model of human hepatocellular carcinoma

For creating metastatic mouse models of human hepatocellular carcinoma (HCC), histologically intact specimens from patients suffering from HCC are implanted directly into the liver of nude mice (Sun et al. 1996). This process allows monitoring of the specimen's orthotopic growth and metastases over time, and provides a means of understanding and predicting clinical behavior of HCC (Fu et al. 1991). To simulate HCC in the mouse, we first artificially created a primary implantation site in the liver of the Digimouse based on published data (Hoffman 1999). The longest diameter of this implanted lesion was approximately 8 mm. Since metastatic lesions on follow-up can also be found within the liver itself, we created one small metastatic lesion (approximately 1.2 mm in diameter) on the liver boundary at about 5 mm from the primary lesion. We assume that Alexa 700 will accumulate at the two sites due to increased blood flow from tumor neovascularization. A representative horizontal section through the CT of the Digimouse showing the simulated spatial distribution of Alexa 700 is shown in figure 5(a). This distribution in reality is in 3D though only 2D sections are shown for visual clarity. For imaging, simulated data were generated using the optical setup in figure 1 and using the method described in section 2.3. Images were reconstructed using the regularized pseudo-inverse method. The SNRs were set to 20 dB (MWI-MD), 27.8 dB (SWI-MD and MWI-AD), and 35.5 dB (SWI-AD) as described in section 2.5. The regularization parameter in each case was chosen from the resolution-variance plot to correspond to equal noise variance. This allowed the noise levels to be matched for the four types of data acquisition.

3. Results

3.1. The SVD study

Our results from the SVD of the four forward models are shown in figure 3. The SWI-AD model has better conditioning compared to other models for higher singular values, however, the drop-off of the spectrum is steep. Therefore, it will tend to be less robust to noise compared to other models. The SWI-MD model has better conditioning than the SWI-AD model implying that there certainly is a reduction in ill-posedness because multispectral detection of emission data was used. The observation that multispectral detection was indeed useful is further strengthened by the comparison between MWI-AD and MWI-MD where the same excitation wavelength bins were used. In this case, the MWI-MD model clearly has better conditioning than MWI-AD.

A comparison between the SWI-AD, SWI-MD and MWI-AD models indicates that although there certainly is an advantage when multispectral detection is used, the improvement in conditioning achieved is less than that achieved through illumination at multiple wavelengths. The MWI-MD model has the best conditioning among all four models indicating that information in both illumination and emission domains need to be exploited for optimal outcomes.

3.2. Resolution-variance comparisons

The results of our resolution-variance analysis are shown in figure 4, where we have plotted the average spatial resolution, measured by the full-width half-maximum of a point spread function, over the 100 representative sources against relative estimator variance as a function of the regularization parameter α. The relative variance in each case is defined as the ratio of the computed variance to the variance of the SWI-AD model at $\alpha = 10^{-13}$. For a constant spatial resolution value and over all values of α, the MWI-MD model has the least variance. This, in turn, implies that for any fixed value of spatial resolution the images reconstructed using the MWI-MD model will deviate least from their mean values compared to other models. Thus, this model provides a more stable solution compared to other models.

The SWI-AD model has the worst resolution-variance characteristics, while the MWI-AD model performs better than the SWI-MD model overall. We observe a relatively large SNR gain (values between 2.5 and 20, with an average of 8) for the MWI-MD-based results compared to those based on MWI-AD. This SNR gain for MWI-MD on an average was close to 20 compared to the SWI-MD results and in the thousands for SWI-AD. Over all variance values, we consistently observe a 0.2–0.3 mm and 0.5–0.6 mm improvement in spatial resolution for the MWI-MD-based results compared to those obtained for the MWI-AD and SWI-MD models respectively at matched noise levels. With respect to SWI-AD, the MWI-MD-based results show an average spatial resolution improvement of close to 1.5 mm. These results validate our findings from the SVD study that multispectral detection is indeed useful, illumination at multiple wavelenghts is better than illumination at a single wavelength, and information from both illumination and emission domains must be used synergistically to obtain the best result.

3.3. Image reconstruction study in a realistic mouse phantom

Results from our reconstruction study are shown in figure 5. In figure 5(b), we show an image reconstructed using the SWI-AD approach. The reconstructed distribution shows only broad similarity to the true distribution from figure 5(a), with the deeper structure and the smaller lesion not visualized. Even in figure 5(c), where a reconstruction result using the SWI-MD approach is shown, superficial parts of the primary site are reconstructed better than the deeper parts. This effect can be attributed to decreased SNR for deep sources and hence, decreased

spatial resolution that consequently, blurs out the signal. Mathematically, noise is able to significantly affect the small singular values which typically carry depth information (Chaudhari 2006). The reconstruction result using the MWI-AD model is shown in figure 5 (d). In this case, deeper sections of the primary lesion appear to be reconstructed better than those in reconstructed images generated from the SWI-MD approach. The best result is obtained using the MWI-MD approach and the corresponding reconstructed source distribution is shown in figure 5(e). The reconstructed image in this case shows the metastatic lesion in addition to the primary lesion. This metastatic lesion is deep in tissue and was not visible in the reconstructed images from the other three models. Thus, MWI-MD approaches provide the best quantitative ability and depth sensitivity (both by-products of improved spatial resolution and robustness to noise), while the SWI-AD model provides the worst.

4. Discussion

The imaging performance using forward models that incorporated excitation at multiple wavelengths was compared to models that used excitation at a single wavelength and achromatic or multispectral detection. Multispectral detection techniques led to better conditioned forward models compared to those that used achromatic detection. Excitation at multiple wavelengths added another favorable dimension to the otherwise ill-posed OFT inverse problem. An imaging study conducted using a realistic mouse model showed the potential of our excitation spectroscopy approach in multispectral OFT for imaging of small lesions deep in tissue. This study also confirmed our findings from SVD and resolution-variance analyses. Because the focus of this paper was spectral-domain analysis, we chose to have the animal surface uniformly illuminated. The conditioning of all our models will improve even further if optimal spatial distributions for the illumination (Joshi et al. 2006b, Deliolanis et al. 2008) are coupled with our spectral approaches.

The proposed method capitalizes on the fact that higher variability in tissue optical properties is observed for illumination photons compared to emission photons. This variability then leads to some amount of independent information in the models and yields better performance for image reconstruction. The results shown in this paper were limited to one representative fluorophore. We anticipate that the benefits of excitation spectroscopy would reduce compared to those shown in this work for fluorescent probes that have their absorption spectrum red-shifted compared to that of Alexa 700. However, even for these probes, there will be higher variability of optical properties for excitation photons compared to emission photons. Thus, MWI-MD approaches will still be valuable. Better results than those shown here may be achieved for probes whose absorption spectra are blue-shifting with respect to that of Alexa 700. However, there will be limited penetration of excitation light in tissue at these wavelenghts. Thus, careful determination of the benefits of the MWI-MD approach is necessary for different probes. We recommend the SVD and resolution-variance analyses as quantitative methods to facilitate this determination.

Imaging systems that are able to measure multispectral emission data have become available commercially. The proposed method additionally requires the capability of illuminating the subject at multiple wavelengths. One possible way of achieving this is by using a broadband light source with a tunable filter (Gao et al. 2004, Leavesley et al. 2008). The tunable filter in this case should ideally have a narrow passband, sharp cutoff, high attenuation in the stop-band, and fast switching times. The broadband source should possess sufficient power so that light levels after filtering are suitable for imaging. A second technique of achieving excitation at multiple wavelengths may involve separate lasers for illumination, but the cost of this setup may be significantly higher.

One limitation of the presented study is that tissue autofluorescence was not taken into account explicitly. Tissue autofluorescence is a function of wavelength (Anderson and Parrish 1981) and thus, the excitation wavelenghts to be used need to be chosen carefully. The influence of autofluorescence on the optical reconstruction result may be reduced by machine learning approaches (Mansfield et al. 2005) or by explicitly accounting for it in the formulation of the forward model. The latter technique needs further investigation.

In this paper, a large number of reconstructed images were needed for our evaluation and thus, we used the direct regularized pseudo-inverse-based solution. The assembly of all the models took close to 5 hours on a Dual Core AMD Opteron™ 2.33 GHz processor. The computation of the SVD for each model took close to 25 min. Additionally, no non-negativity constraint was enforced on the solution. Fast iterative approaches for on-the-fly computation of the forward models and reconstructed images that incorporate non-negativity constraints have been investigated (Ahn et al. 2008a, Ahn et al. 2008b). Our proposed method will greatly benefit from these developments.

5. Conclusions

We have proposed a method for OFT that utilizes excitation spectroscopic information in addition to the detection of optical multispectral emission data. We compared this approach with conventional approaches that use only illumination at a single wavelength with either achromatic or multispectral data using one representative fluorescent dye (Alexa 700®). Studies involving singular value analyses and spatial resolution versus variance curves unanimously show benefits of using our approach of excitation spectroscopy. Our results in a simulated realistic mouse model of human hepatocellular carcinoma show that the proposed approach allows for exploiting both excitation and emission domain information to reduce the ill-posedness of the OFT inverse problem. Our results also indicate that for the Alexa 700® dye, excitation spectroscopy was better suited for extracting depth information compared to emission spectroscopy (measurement of multispectral emission data). This should be true for NIR probes in general, since the excitation band is blue-shifted compared to the emission band and thus, more depth-dependent spectral information will be available in the excitation band. There are three critical limitations of this study. Firstly, tissue autofluorescence has not been taken into consideration. Secondly, the diffusion approximation to the RTE used for forward model generation may not be accurate in certain anatomical regions of the animal. Thirdly, we have demonstrated our method for only one representative dye and thus, our quantitative results have limited scope. Careful determination of the benefits of the proposed approach is necessary for different probes.

Acknowledgments

Appendix

Appendix A

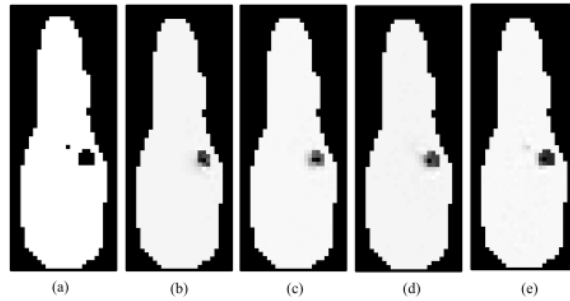## Reconstructed optical images without any thresholding

Figure A1 Reconstructed images from figure 5 without thresholding; (a) the simulated distribution of Alexa 700, (b), (c), (d) and (e) reconstructed images using the SWI-AD, SWI-MD, MWI-AD and the MWI-MD models respectively. The color scale used for these images is the inverse of the conventional gray scale.

References

Adams K, Ke S, Kwon S, Liang F, Fan Z, Lu Y, Hirschi K, Mawad M, Barry M, Sevick-Muraca E. Comparison of visible and near-infrared wavelength-excitable fluorescent dyes for molecular imaging of cancer. Journal of Biomedical Optics 2007;12:024017. [PubMed: 17477732]

Ahn S, Chaudhari AJ, Darvas F, Bouman CA, Leahy RM. Fast iterative image reconstruction methods for fully 3D multispectral bioluminescence tomography. Phys. Med. Biol 2008a;53:3921–3942. [PubMed: 18591735]

Ahn S, Dutta J, Chaudhari AJ, Leahy RM. Computationally efficient image reconstruction methods for multispectral optical fluorescence tomography using FEM-based forward models. Abstract Book Joint Molecular Imaging Conf 2008b:329–330.

Alessio, A.; Kinahan, P. PET Image Reconstruction, Nuclear Medicine. Vol. 2nd edn. Elsevier; 2006.

Alexandrakis G, Rannou FR, Chatziioannou AF. Tomographic bioluminescence imaging by use of a combined optical-PET (OPET) system: a computer simulation feasibility study. Physics in Medicine and Biology 2005;50(17):4225–4241. [PubMed: 16177541]

Anderson R, Parrish J. The Optics of Human Skin. Journal of Investigative Dermatology 1981;77(1):13–19. [PubMed: 7252245]

Arridge S. Optical tomography in medical imaging. Inverse Problems 1999;15(2):41–93.

Arridge SR, Hebden JC. Optical imaging in medicine:II. Modelling and reconstruction. Physics in Medicine and Biology 1997;42(5):841–853. [PubMed: 9172263]

Arridge SR, Schweiger M, Hiroaka M, Delpy DT. A finite element approach for modeling photon transport in tissue. Phys. Med. Biol 1993;20(2):299–309.

Axelsson J, Svensson J, Andersson-Engels S. Spatially varying regularization based on spectrally resolved fluorescence emission in fluorescence molecular tomography. Optics Express 2007;15(21):13574–13584. [PubMed: 19550625]

Bargo P, Prahl SA, Goodell TT, Sleven RA, Koval G, Blair G, Jacques SL. In vivo determination of optical properties of normal and tumor tissue with white light reflectance and an empirical light transport model during endoscopy. Journal of Biomedical Optics 2005;10(3):034018. [PubMed: 16229662]

Boas D, Brooks DH, Miller EL, DiMarzio CA, Kilmer M, Gaudette RJ, Zhang Q. Imaging the body with diffuse optical tomography. IEEE Signal Processing Magazine 2001;18(6):57–75.

Chance B. Optical method. Annu. Rev. Biophys. Biophys. Chem 1991;20:1–28. [PubMed: 1867711]

Chang J, Graber HL, Barbour RL. Imaging of fluorescence in highly scattering media. IEEE Transactions on Biomedical Engineering 1997;44(9):810–822. [PubMed: 9282473]

Chaudhari, AJ. PhD thesis. University of Southern California; 2006. Hyperspectral and multispectral optical bioluminescence and fluorescence tomography in small animal imaging.

Chaudhari AJ, Darvas F, Bading JR, Moats RA, Conti PS, Smith DJ, Cherry SR, Leahy RM. Hyperspectral and multispectral bioluminescence optical tomography for small animal imaging. Physics in Medicine and Biology 2005;50(23):5421–5441. [PubMed: 16306643]

Chaudhari AJ, Joshi AA, Darvas F, Leahy RM. A method for atlas-based volumetric registration with surface constraints for optical bioluminescence tomography in small animal imaging. Proc.SPIE Medical Imaging 2008 ; Physics of Medical Imaging 2007;Vol. 6510:651024.

Cheong WF, Prahl SA, Welch AJ. A review of the optical properties of biological tissues. IEEE Journal of Quantum Electronics 1990;26:2166–2185.

Cherry SR. In vivo molecular and genomic imaging: new challenges for imaging physics. Physics in Medicine and Biology 2004;49(3):R13–R48. [PubMed: 15012005]

Cong A, Wang G. A finite-element-based reconstruction method for 3D fluorescence tomography. Optics Express 2005;13:9847–9857. [PubMed: 19503194]

Cong AX, Wang G. Multispectral bioluminescence tomography: methodology and simulation. International Journal of Biomedical Imaging 2006;2006Article ID 57614

Dahlquist, G.; Bjorck, A. Numerical Methods in Scientific Computing: Volume 1. Philadelphia, PA, USA: Society for Industrial and Applied Mathematics; 2008.

Dehghani H, Arridge S, Schweiger M, Delpy D. Optical tomography in the presence of void regions. Journal of the Optical Society of America A 2000;17(9):1659–1670.

Dehghani H, Davis SC, Jiang S, Pogue BW, Paulsen KD, Patterson MS. Spectrally resolved bioluminescence optical tomography. Optics Letters 2006;3:365–367. [PubMed: 16480210]

Deliolanis N, Kasmieh R, Wurdinger T, Tannous B, Shah K, Ntziachristos V. Performance of the red-shifted fluorescent proteins in deep-tissue molecular imaging applications. Journal of Biomedical Optics 2008;13:044008. [PubMed: 19021336]

Dogdas B, Stout D, Chatziioannou AF, Leahy RM. Digimouse: a 3D whole body mouse atlas from CT and cryosection data. Physics in Medicine and Biology 2007;52(3):577–587. [PubMed: 17228106]

Fu X, Besterman J, Monosov A, Hoffman R. Models of human metastatic colon cancer in nude mice orthotopically constructed by using histologically intact patient specimens. Proceedings of the National Academy of Sciences 1991;88(20):9345–9349.

Gao X, Cui Y, Levenson R, Chung L, Nie S. In vivo cancer targeting and imaging with semiconductor quantum dots. Nature Biotechnology 2004;22:969–976.

Giepmans BNG, Adams SR, Ellisman MH, Tsien RY. The fluorescent toolbox for assessing protein location and function. Science 2006;312(5771):217–224. [PubMed: 16614209]

Godavarty A, Zheng C, Eppstein MJ, Sevick-Muraca EM. Fluorescence enhanced optical imaging of large phantoms using single and simulteneous dual point illumination geometries. Medical Physics 2004;31(2):183–190. [PubMed: 15000603]

Guven, M.; Yazici, B.; Ntziachristos, V. Fluorescence optical tomography with a priori information. Vol. Vol. 6431. SPIE; 2007.

Haskell RC, Svaasand LO, Tsay TT, Feng TC, McAdams MS, Tromberg BJ. Boundary conditions for the diffusion equation in radiative transfer. J. Opt. Soc. Am. A 1994;11(10):2727–2740.

Hassan M, Riley J, Chernomordik V, Smith P, Pursley R, Lee SB, Capala J, Gandjbakhche AH. Fluorescence lifetime imaging system for in vivo studies. Molecular Imaging 2007;6(4):229–236. [PubMed: 17711778]

Hielscher A. Optical tomographic imaging of small animals. Current opinion in biotechnology 2005;16 (1):79–88. [PubMed: 15722019]

Hoffman R. Orthotopic metastatic mouse models for anticancer drug discovery and evaluation: a bridge to the clinic. Investigational New Drugs 1999;17(4):343–360. [PubMed: 10759402]

Joshi A, Bangerth W, Sevick-Muraca EM. Adaptive finite element based tomography for fluorescence optical imaging in tissue. Optics Express 2004;12:5402–5417. [PubMed: 19484100]

Joshi A, Bangerth W, Hwang K, Rasmussen JC, Sevick-Muraca EM. Fully adaptive FEM based fluorescence optical tomography from time-dependent measurements with area illumination and detection. Medical Physics 2006a;33:1299. [PubMed: 16752565]

Joshi A, Bangerth W, Sevick-Muraca E. Non-contact fluorescence optical tomography with scanning patterned illumination. Optics Express 2006b;14(14):6516–6534. [PubMed: 19516829]

Joshi A, Rasmussen J, Sevick-Muraca E, Wareing T, McGhee J. Radiative transport-based frequency-domain fluorescence tomography. Physics in Medicine and Biology 2008;53(8):2069–2088. [PubMed: 18364555]

Klose AD, Hielscher AH. Fluorescence tomography with simulated data based on the equation of radiative transfer. Optics Letters 2003;28(12):1019–1021. [PubMed: 12836765]

Klose A, Ntziachristos V, Hielscher A. The inverse source problem based on the radiative transfer equation in optical molecular imaging. Journal of Computational Physics 2005;202(1):323–345.

Koenig A, Herve L, Josserand V, Berger M, Boutet J, da Silva A, Dinten J, Peltie P, Coll J, Rizo P. In vivo mice lung tumor follow-up with fluorescence diffuse optical tomography. Journal of Biomedical Optics 2008;13(1)

Kumar ATN, Raymond SB, Dunn AK, Bacskai BJ, Boas DA. A time domain fluorescence tomography system for small animal imaging. IEEE Transactions on Medical Imaging 2008;27(8):1152–1163. [PubMed: 18672432]

Kuo C, Coquoz O, Troy TL, Xu H, Rice BW. Three-dimensional reconstruction of in vivo bioluminescent sources based on multispectral imaging. Journal of Biomedical Optics 2007;12(2):024007. [PubMed: 17477722]

Lasser T, Soubret A, Ripoll J, Ntziachristos V. Surface reconstruction for free-space 360° fluorescence molecular tomography and the effects of animal motion. IEEE Transactions on Medical Imaging 2008;27(2):188–194. [PubMed: 18334440]

Leavesley S, Jiang Y, Patsekin V, Rajwa B, Robinson J. An excitation wavelength–scanning spectral imaging system for preclinical imaging. Review of Scientific Instruments 2008;79:023707. [PubMed: 18315305]

Luker G, Luker K. Optical imaging: current applications and future directions. Journal of Nuclear Medicine 2008;49(1):1–4. [PubMed: 18077528]

Lv, Y.; Tian, J.; Cong, W.; Wang, G.; Kumar, D. MicroCT-guided bioluminescence tomography based on the adaptive finite element tomographic algorithm; IEEE Engineering in Medicine and Biology Society, 28th Annual Meeting; 2006. p. 381-384.

Mansfield J, Gossage K, Hoyt C, Levenson R. Autofluorescence removal, multiplexing, and automated analysis methods for in-vivo fluorescence imaging. Journal of Biomedical Optics 2005;10:041207.

Massoud TF, Gambhir SS. Molecular imaging in living subjects: seeing fundamental biological processes in a new light. Genes Dev 2003;17(5):545–580. [PubMed: 12629038]

Meyer H, Garofalakis A, Zacharakis G, Psycharakis S, Mamalaki C, Kioussis D, Economou E, Ntziachristos V, Ripoll J. Noncontact optical imaging in mice with full angular coverage and automatic surface extraction. Applied Optics 2007;46(17):3617–3627. [PubMed: 17514324]

Milstein AB, Oh S, Webb KJ, Bouman CA, Zhang Q, Boas DA, Millane RP. Fluorescence optical diffusion tomography. Applied Optics 2003;42(16):3081–3094. [PubMed: 12790460]

Neefjes J, Dantuma NP. Fluorescent probes for proteolysis: Tools for drug discovery. Nature Reviews Drug Discovery 2004;3:58–69.

Ntziachristos V. Fluorescence molecular tomography. The Annual Review of Biomedical Engineering 2006;8:1–33.

Ntziachristos V, Ripoll J, Wang LV, Weissleder R. Looking and listening to light: the evolution of whole-body photonic imaging. Nature Biotechnology 2005;23:313–320.

Ntziachristos V, Ripoll J, Weissleder R. Would near-infrared fluorescence signals propagate through large human organs for clinical studies? Optics Letters 2002;27(5):333–335. [PubMed: 18007794]

Ntziachristos V, Schellenberger EA, Ripoll J, Yessayan D, Graves E, Bogdanov A Jr, Josephson L, Weissleder R. Visualization of antitumor treatment by means of fluorescence molecular tomography with an annexin V-Cy5.5 conjugate. PNAS 2004;101(33):12294–12299. [PubMed: 15304657]

Ntziachristos V, Weissleder R. Experimental three-dimensional fluorescence reconstruction of diffuse media by use of a normalized born approximation. Optics Letters 2001;26(2):893–895. [PubMed: 18040483]

Ntziachristos V, Weissleder R. Charge-coupled-device based scanner for tomography of fluorescent near-infrared probes in turbid media. Medical Physics 2002;29(5):803–809. [PubMed: 12033576]

Paithankar DY, Chen AU, Pogue BW, Patterson MS, Sevick-Muraca EM. Imaging of fluorescent yield and lifetime from multiply scattered light reemitted from random media. Applied Optics 1997;36 (10):2260–2272. [PubMed: 18253202]

Patterson MS, Pogue BW. Mathematical model for time-resolved and frequency-domain fluorescence spectroscopy in biological tissues. Applied Optics 1994;33:1963–1974.

Patterson MS, Wilson BC, Wyman DR. The propagation of optical radiation in tissue 1: models of radiation transport and their application. Lasers Med. Sci 1992;6:155–168.

Patwardhan S, Bloch S, Achilefu S, Culver J. Time-dependent whole-body fluorescence tomography of probe bio-distributions in mice. Optics Express 2005;13(7):2564–2577. [PubMed: 19495147]

Paulsen KD, Jiang H. Spatially-varying optical property reconstructions using a finite element diffusion equation approximation. Medical Physics 1995;22:691–701. [PubMed: 7565358]

Pinaud F, Michalet X, Bentolila LA, Tsay JM, Doose S, Li JJ, Iyer G, Weiss S. Advances in fluorescence imaging with quantum dot bio-probes. Biomaterials 2006;27(9):1679–1687. [PubMed: 16318871]

Pogue BW, Gibbs SL, Chen B, Savellano M. Fluorescence imaging in vivo: raster scanned point-source imaging provides more accurate quantification than broad beam geometries. Technology in Cancer Research and Treatment 2004;3(1):15–21. [PubMed: 14750889]

Ren K, Bal G, Hielscher A. Transport-and diffusion-based optical tomography in small domains: a comparative study. Applied Optics 2007;46(27):6669–6679. [PubMed: 17882287]

Reynolds JS, Thompson CA, Webb KJ, D Ben-Amotz FPL. Frequency domain modeling of reradiation in highly scattering media. Applied Optics 1997;36:2252–2259. [PubMed: 18253201]

Rice BW, Cable MD, Nelson MB. In vivo imaging of light-emitting probes. Journal of Biomedical Optics 2001;6(4):432–440. [PubMed: 11728202]

Rice, BW.; Xu, H.; Kuo, C. Surface construction using combined photographic and structured light information. Patent Application. 0268153. 2006.

Ripoll J, Ntziachristos V. Imaging scattering media from a distance: theory and applications of non-contact optical tomography. Mod. Phys. Lett. B 2004;18(28–29):1403–1431.

Ripoll J, Schulz RB, Ntziachristos V. Free-space propagation of diffuse light: theory and experiments. Phys. Rev. Lett 2003;91:103901. [PubMed: 14525478]

Roy R, Godavarty A, Sevick-Muraca E. Fluorescence-enhanced optical tomography using referenced measurements of heterogeneous media. IEEE Trans Med Imaging 2003;22(7):824–836. [PubMed: 12906236]

Roy R, Godavarty A, Sevick-Muraca EM. Fluorescence-enhanced optical tomography of a large tissue phantom using point illumination geometries. Journal of Biomedical Optics 2006;11:044007. [PubMed: 16965164]

Schulz R, Ripoll J, Ntziachristos V. Experimental fluorescence tomography of tissues with noncontact measurements. IEEE Transactions on Medical Imaging 2004;23(4):492–500. [PubMed: 15084074]

Soubret A, Ripoll J, Ntziachristos V. Accuracy of fluorescent tomography in the presence of heterogeneities: study of the normalized Born ratio. IEEE Trans Med Imaging 2005;24(10):1377–1386. [PubMed: 16229423]

Sun F, Tang Z, Liu K, Xue O, Gao D, Yu Y, Zhou X, Ma Z. Metastatic models of human liver cancer in nude mice orthotopically constructed by using histologically intact patient specimens. Journal of Cancer Research and Clinical Oncology 1996;122(7):397–402. [PubMed: 8690749]

Swartling J, Svensson J, Bengtsson D, Terike K, Andersson-Engels S. Fluorescence spectra provide information on the depth of fluorescent lesions in tissue. Applied Optics 2005;44(10):1934–1941. [PubMed: 15813529]

Tikhonov, A.; Arsenin, V. Solution of ill-posed problems. New York: Wiley; 1977.

Wang G, Cong W, Durairaj K, Qian X, Shen H, Sinn P, Hoffman E, McLennan G, Henry M. In vivo mouse studies with bioluminescence tomography. Optics Express 2006;14:17.

Weber W, Czernin J, Phelps M, Herschman H, et al. Technology Insight: novel imaging of molecular targets is an emerging area crucial to the development of targeted drugs. Nature Clinical Practice Oncology 2008;5(1):44.

Weissleder R, Ntziachristos V. Shedding light onto live molecular targets. Nature Medicine 2003;9(1): 123–128.

Weissleder R, Tung CH, Mahmood U, Bogdanov A. In vivo imaging of tumors with protease-activated near-infrared fluorescent probes. Nature Biotechnology 1999;17:375–378.

Zacharakis G, Kambara H, Shih H, Ripoll J, Grimm J, Saeki Y, Weissleder R, Ntziachristos V. Volumetric tomography of fluorescent proteins through small animals in vivo. Proc Natl Acad Sci U S A 2005;102 (51):18252–18257. [PubMed: 16344470]

Zavattini G, Vecchi S, Mitchell G, Weisser U, Leahy RM, Pichler BJ, Smith DJ, Cherry SR. A hyperspectral fluorescence system for 3D in vivo optical imaging. Physics in Medicine and Biology 2006;51(8):2029–2043. [PubMed: 16585843]
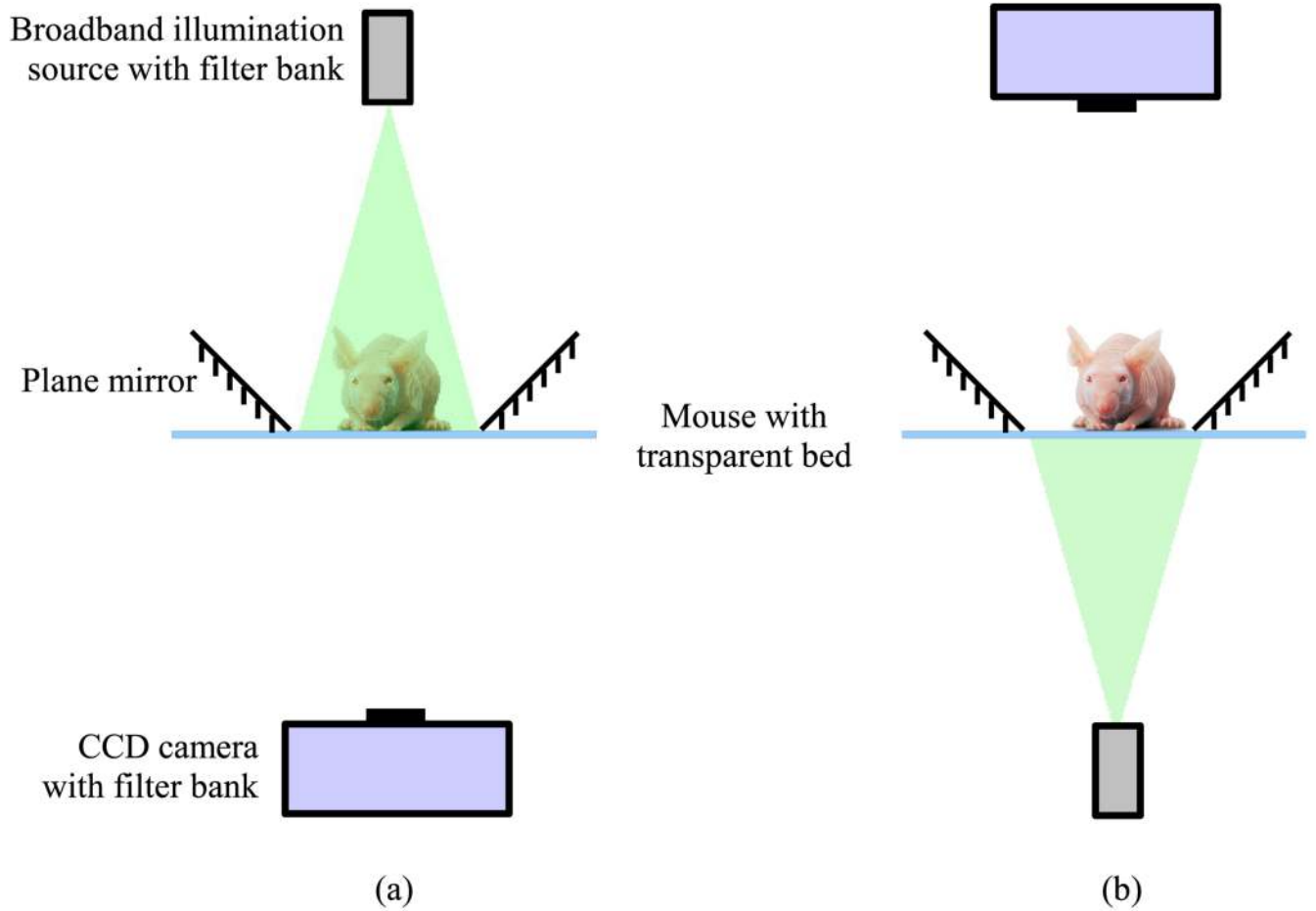
Figure 1.
Optical setup used for simulation experiments; (a) the first configuration with illumination on the top surface and detection from the bottom surface, (b) the second configuration with illumination on the bottom surface and detection from the top and sides. Multiple views are necessary for tomography and are acquired by the two-mirror setup (Chaudhari 2006).
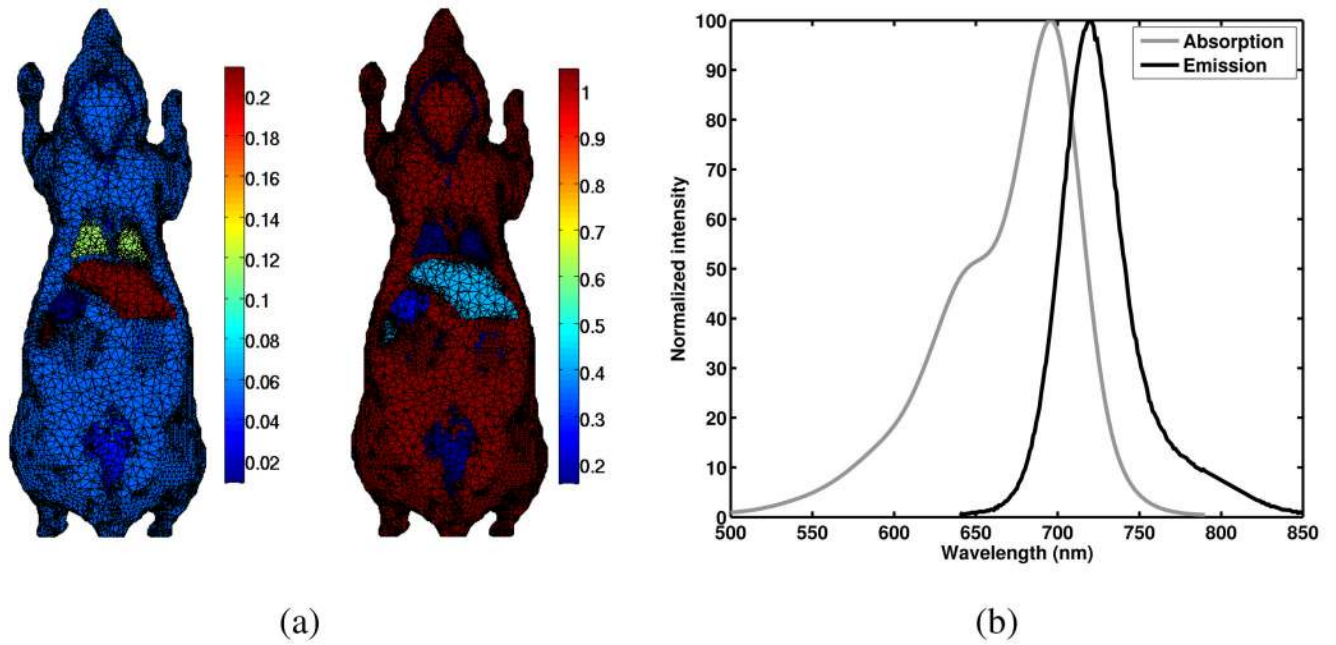
Figure 2.
Assignment of optical properties and the absorption and emission spectra of Alexa 700®; (a) horizontal cut through the 3D tetrahedralmesh representation of the Digimouse atlas showing the assignment of the absorption coefficient (mm^{-1}) (left) and the optical diffusion coefficient (mm^{-1}) (right) to internal organs at wavelength 760 nm, (b) the characteristic absorption and emission spectra of the Alexa 700® dye. For experiments in this paper, the 580–680 nm band was used for excitation while the 700–800 nm band was used for multispectral data acquisition.
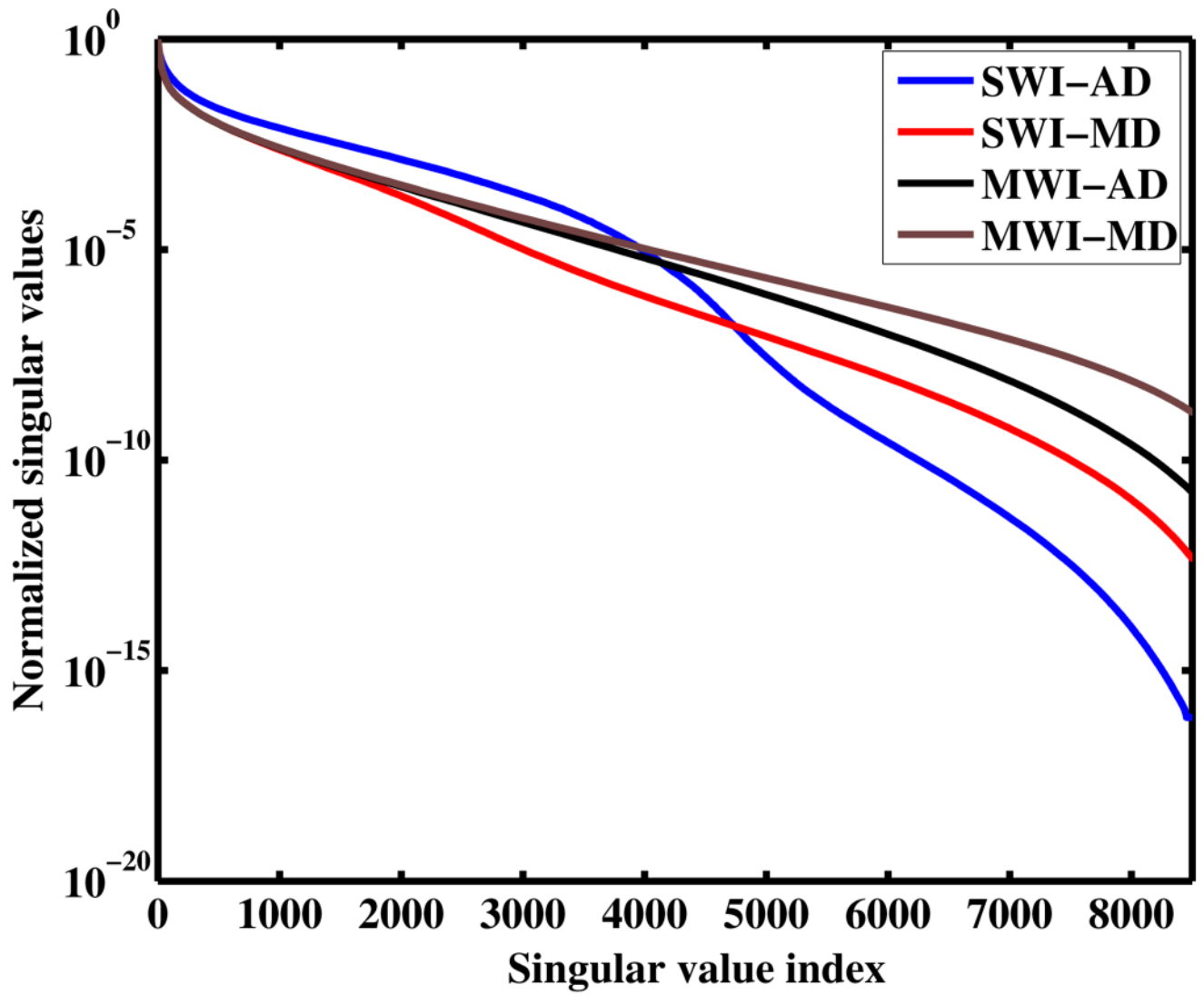
Figure 3.
Comparison of singular value spectra for the forward models. For the SWI-AD model, we have used six times more surface detectors for a fair comparison.
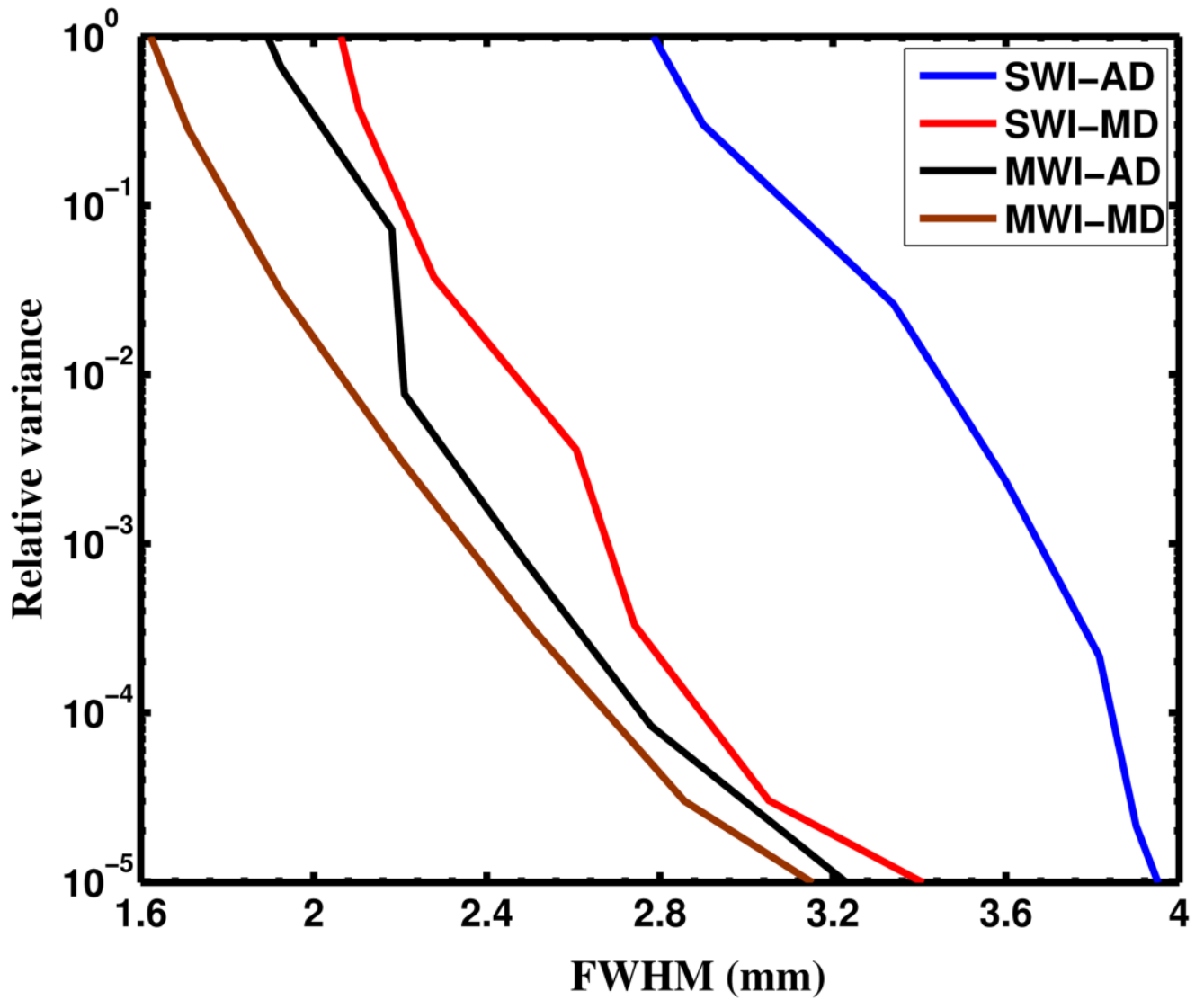
Figure 4.
Average spatial resolution versus relative estimator variance as a function of regularization parameter α. Relative variance is the ratio of the computed variance to the variance of the SWI-AD model at $\alpha = 10^{-13}$
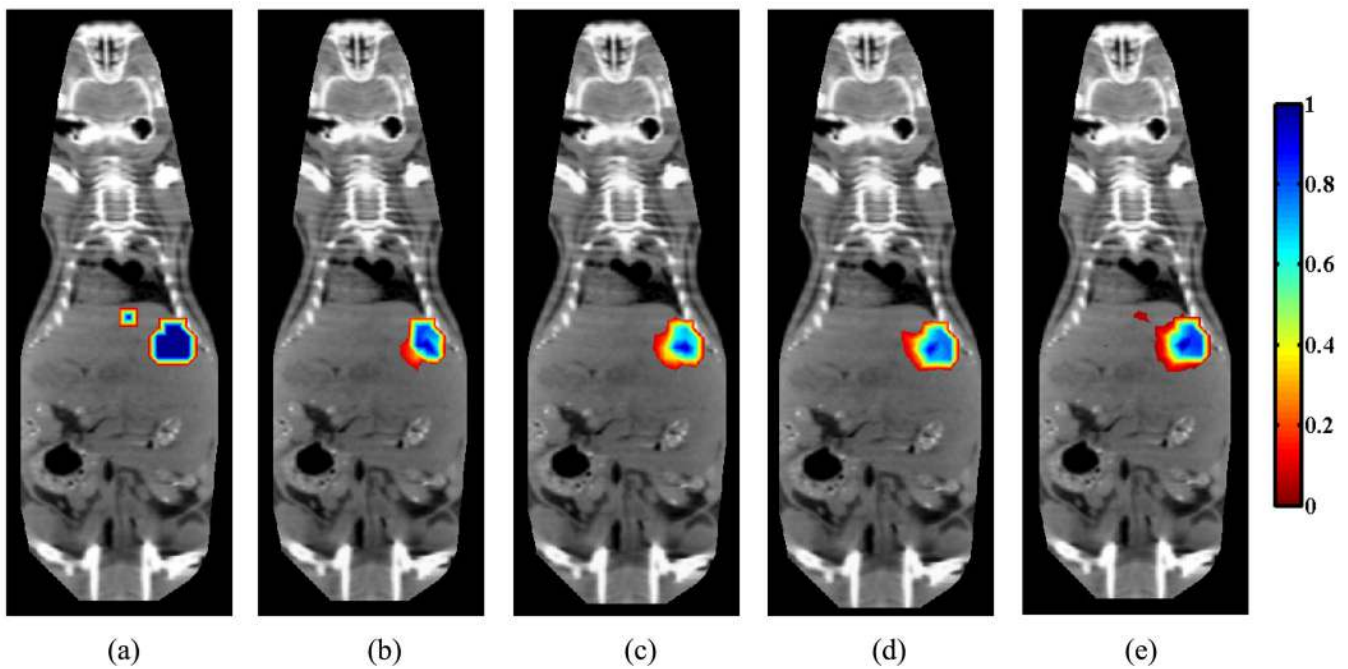
Figure 5.
Reconstruction from noisy data in a mouse model of human hepatocellular carcinoma; (a) a representative horizontal section from the CT of the Digimouse (gray scale) with the simulated distribution of the Alexa dye overlaid (in color), reconstructed images obtained from using the SWI-AD (b), SWI-MD (c), MWI-AD (d) and the MWI-MD (e) models overlaid on the CT section. The regularization parameter in each case was chosen from the resolution-variance plots to correspond to equal noise variance. The reconstructed optical images were linearly interpolated to match the CT image resolution. Reconstructed values greater than or equal to 10% of the maximum value are displayed. Reconstructed images without interpolation and thresholding are shown in figure A1

Table 1

Forward models used for the singular value decomposition (SVD) study, spatial resolution versus variance analyses and imaging comparisons. These models were chosen to allow for detailed investigation of both excitation and emission domains.

Model name	Abbreviation
Single wavelength illumination - achromatic detection	SWI-AD
Single wavelength illumination - multispectral detection	SWI-MD
Multiple wavelength illumination - achromatic detection	MWI-AD
Multiple wavelength illumination - multispectral detection	MWI-MD

Table 2

Formulae for the computation of the optical forward model

Model	Derived formulae	Size
SWI-AD	$\mathbf{X}_i^{SWI-AD} = s(\lambda_i)\left(\sum_{j=1}^{z} t(\lambda_j)\,\mathbf{X}_{ij}\right)$	$\mathbb{R}^{m \times n}$
SWI-MD	$\mathbf{X}_i^{SWI-MD} = \left[\, s(\lambda_i)\, t(\lambda_1)\, \mathbf{X}_{i1}^{T}\ \ s(\lambda_i)\, t(\lambda_2)\, \mathbf{X}_{i2}^{T}\ \cdots\ s(\lambda_i)\, t(\lambda_z)\, \mathbf{X}_{iz}^{T} \right]^{T}$	$\mathbb{R}^{zm \times n}$
MWI-AD	$\mathbf{X}^{MWI-AD} = \left[(\mathbf{X}_1^{SWI-AD})^{T}\ (\mathbf{X}_2^{SWI-AD})^{T}\ \cdots\ (\mathbf{X}_y^{SWI-AD})^{T} \right]^{T}$	$\mathbb{R}^{ym \times n}$
MWI-MD	$\mathbf{X}^{MWI-MD} = \left[(\mathbf{X}_1^{SWI-MD})^{T}\ (\mathbf{X}_2^{SWI-MD})^{T}\ \cdots\ (\mathbf{X}_y^{SWI-MD})^{T} \right]^{T}$	$\mathbb{R}^{yzm \times n}$